

Development and Initial Results of a Brain PET Insert for Simultaneous 7-Tesla PET/MRI Using an FPGA-Only Signal Digitization Method

Jun Yeon Won¹, Haewook Park¹, *Graduate Student Member, IEEE*,
 Seungeun Lee¹, *Graduate Student Member, IEEE*, Jeong-Whan Son, *Member, IEEE*,
 Yina Chung, Guen Bae Ko¹, Kyeong Yun Kim, Junghyun Song¹, Seongho Seo, *Member, IEEE*,
 Yeunchul Ryu¹, Jun-Young Chung¹, and Jae Sung Lee¹, *Senior Member, IEEE*

Abstract—In study, we developed a positron emission tomography (PET) insert for simultaneous brain imaging within 7-Tesla (7T) magnetic resonance (MR) imaging scanners. The PET insert has 18 sectors, and each sector is assembled with two-layer depth-of-interaction (DOI)-capable high-resolution block detectors. The PET scanner features a 16.7-cm-long axial field-of-view (FOV) to provide entire human brain images without bed movement. The PET scanner early digitizes a large number of block detector signals at a front-end data acquisition (DAQ) board using a novel field-programmable gate array (FPGA)-only signal digitization method. All the digitized PET data from the front-end DAQ boards are transferred using gigabit transceivers via non-magnetic high-definition multimedia interface (HDMI) cables. A back-end DAQ system provides a

common clock and synchronization signal for FPGAs over the HDMI cables. An active cooling system using copper heat pipes is applied for thermal regulation. All the 2.17-mm-pitch crystals with two-layer DOI information were clearly identified in the block detectors, exhibiting a system-level energy resolution of 12.6%. The PET scanner yielded clear hot-rod and Hoffman brain phantom images and demonstrated 3D PET imaging capability without bed movement. We also performed a pilot simultaneous PET/MR imaging study of a brain phantom. The PET scanner achieved a spatial resolution of 2.5 mm at the center FOV (NU 4) and a sensitivity of 18.9 kcps/MBq (NU 2) and 6.19% (NU 4) in accordance with the National Electrical Manufacturers Association (NEMA) standards.

Index Terms—Brain PET, DAQ, FPGA, NEMA, simultaneous PET/MRI.

Manuscript received January 11, 2021; revised February 16, 2021; accepted February 21, 2021. Date of publication February 24, 2021; date of current version June 1, 2021. This work was supported in part by the National Research Foundation of Korea (NRF) through the Ministry of Science and ICT under Grant NRF-2014M3C7034000 and Grant NRF-2016R1A2B3014645 and in part by the Ministry of Education under Grant NRF-2018R1D1A1B07045559. (*Jun Yeon Won and Haewook Park contributed equally to this work.*) (*Corresponding author: Jae Sung Lee.*)

Jun Yeon Won is with the Medical Research Center, Institute of Radiation Medicine, Seoul National University College of Medicine, Seoul 03080, South Korea (e-mail: wnsus1029@snu.ac.kr).

Haewook Park and Seungeun Lee are with the Department of Nuclear Medicine and Biomedical Sciences, Seoul National University College of Medicine, Seoul 03080, South Korea (e-mail: phw1235@snu.ac.kr; seungeun058@gmail.com).

Jeong-Whan Son, Yina Chung, Guen Bae Ko, and Kyeong Yun Kim are with Brightonix Imaging Inc., Seoul 04782, South Korea (e-mail: sonjohn@snu.ac.kr; ychung@brtnx.com; gbko@brtnx.com; leo.kim@brtnx.com).

Junghyun Song is with the Neuroscience Research Institute, Gachon University, Incheon 21565, South Korea (e-mail: christmas2558@gmail.com).

Seongho Seo is with the Department of Neuroscience, College of Medicine, Gachon University, Incheon 21565, South Korea, and also with the Department of Electronic Engineering, College of Appenzeller, Pai Chai University, Daejeon 35345, South Korea (e-mail: dansoc@gmail.com).

Yeunchul Ryu is with the Department of Radiological Science, College of Health Science, Gachon University, Incheon 21936, South Korea (e-mail: yeunchul.ryu@gachon.ac.kr).

Jun-Young Chung is with the Department of Neuroscience, College of Medicine, Gachon University, Incheon 21565, South Korea (e-mail: jychung@gachon.ac.kr).

Jae Sung Lee is with the Department of Nuclear Medicine, Seoul National University College of Medicine, Seoul 03080, South Korea (e-mail: jaes@snu.ac.kr).

Digital Object Identifier 10.1109/TMI.2021.3062066

I. INTRODUCTION

POSITRON emission tomography (PET) allows for quantitative measurement of the spatiotemporal distribution of radiotracers. To achieve a fine spatial resolution and high sensitivity, most modern PET scanners are mostly equipped with small-sized high-aspect-ratio crystals [1]–[3] and have a long axial coverage [4]–[7]. The time-of-flight (TOF) information provided by the PET scanners with advanced analog and digital circuits further improves the quality of reconstructed PET images [7]–[10].

The simultaneous operation of PET and magnetic resonance imaging (PET/MRI) scanners enables better spatiotemporal correlation between the functional and anatomical data from both imaging modalities [11], [12]. In addition, PET/MRI yields less radiation exposure and features a superior soft-tissue contrast than PET/computed tomography (CT), resulting in better diagnostic performance in various applications despite the fact that attenuation correction in PET/MRI is more complex than the PET/CT [12]–[14].

One of the approaches to developing the PET/MRI scanners was to utilize optical fibers. The optical fiber made it possible to transfer scintillation photons to the photomultiplier tubes (PMTs) placed away from the scintillation crystals, thereby preventing the influence of the strong static magnetic field on the PET system [15], [16]. However, the transfer of scintillation lights through the optical fibers resulted in the

degradation of energy and timing performances caused by the significant light loss during the light transfer.

Solid-state photodetectors (SSPDs) have allowed the direct coupling of scintillation crystals to the photosensors in the PET/MRI [17] or coupling between them with short optical fiber bundles [18], [19] as an SSPD can operate within a strong static magnetic field without output signal distortion [20].

Avalanche photodiodes (APDs) have facilitated hybrid imaging with simultaneous PET/MRI scanners [21], [22]. An APD-based brain PET system was integrated with 3-Tesla and 9.4-Tesla MRI scanners [23], [24], demonstrating the potential clinical usefulness of PET/MRI. However, a low intrinsic gain of APDs was a critical drawback for developing advanced simultaneous PET/MRI scanner with a good timing resolution.

Therefore, silicon photomultiplier (SiPM) is now most widely used for PET/MRI hardware development as it features a high intrinsic gain of output signals that enhances the TOF measurement capability. However, the SiPM-based PET system suffers from the burden of a large number of readout channels due to the high granularity of SiPMs. Developing a simultaneous PET/MRI system is even more challenging because the PET detectors should meet additional space and power constraints, being placed between the radio-frequency (RF) and gradient coils of MRI scanners [11], [12].

One solution to overcome the space and power constraints is to place the PET data acquisition (DAQ) system outside of the MRI bore and subsequently transfer analog signals from the SiPMs to the DAQ system through shielded cables [3], [25]–[29]. However, the performance of the PET scanner can be degraded as the analog signals are not properly protected from the RF and gradient pulses. This method also requires a large number of interconnections between SiPMs and DAQ systems.

Application-specific integrated circuits (ASICs) have been developed and adopted in various PET/MRI scanners [30]–[33] to address the space and power constraints [34]–[37]. However, ASICs require dedicated FPGA-based DAQ systems to collect PET data and control the operation. In addition, the development of PET scanners with off-the-shelf ASICs has several limitations because the detector design and FPGA should be compatible with ASICs.

The proposed FPGA-only DAQ system uses programmable ports to digitize analog PET signals by configuring ports with low-voltage differential signaling input receivers [38]–[41] or single-ended memory interface (SeMI) input receivers [42], [43]. Therefore, compared to the ASIC, the FPGA-only DAQ system features a relatively high degree-of-freedom for designing the PET DAQ system. Furthermore, a high-speed data transfer module and on-line coincidence processing unit can be implemented within the same FPGA using a built-in serial gigabit transceiver (GT) and logic resources.

In this study, we developed a high-resolution and high-sensitivity brain PET scanner using FPGA-only DAQ systems. The FPGA-only DAQ systems provide an all-in-one solution to digitize SiPM signals using SeMI input receivers and transfer the digitized data using serial GT through a 20-m

high-definition multimedia interface (HDMI) cable. In addition, the back-end DAQ module synchronizes all front-end DAQ boards by providing a common clock and synchronization signals through the HDMI cables. The back-end DAQ system identifies the coincidence events from unsorted single events and subsequently transfers them to a personal computer (PC) through a gigabit Ethernet.

We evaluated the performances of the DAQ systems, block detectors, and PET scanner. We also obtained initial phantom images to demonstrate the benefits of the high-resolution and high-sensitivity PET scanner. Furthermore, we conducted a pilot simultaneous PET/MRI study.

II. 7T MRI-COMPATIBLE BRAIN PET SYSTEM

A. System Overview

The brain PET scanner comprising a PET insert and back-end DAQ system was developed for simultaneous imaging with a whole-body 7-Tesla (7T) MRI scanner (7T Magnetom, Siemens Healthineers) installed at Gachon University. Considering the available bore opening with a height of 45.2 cm of the 7T MRI scanner, we designed the brain PET insert that features an inner bore size and height of 33.0 and 43.7 cm (Fig. 1) to be inserted into the 7T MRI system. The brain PET scanner is wide and sufficiently long to scan the entire human brain without moving the bed or scanner, and it features a transverse and axial field-of-view (FOV) of 25.6 and 16.7 cm, respectively.

The PET insert has 18 sectors, and each sector consists of block detectors, an analog front-end board (FEB), and a front-end DAQ board (Fig. 2). Each sector is housed in a Faraday box assembled using a two-layer printed circuit board. The thickness of each copper layer is 18 μm [44]. Staggered slits are added along the axial direction to reduce the eddy current.

To reduce the number of interconnections between the PET insert and back-end DAQ system, all the sectors are grouped in pairs that share the HDMI cable, as illustrated in Fig. 3. Thus, the total number of sector groups is nine. The block detector generates four energy signals and one timing signal to provide position, energy, and timing information. The analog FEB supports 16 block detectors at maximum, and it amplifies all the 64 analog signals and generates 16 digital timing pulses. The front-end DAQ board digitizes and processes energy and timing signals at their early stages (i.e. early digitization) and subsequently transfers them to the back-end DAQ system. The back-end DAQ system distributes clock and synchronization signals to the front-end DAQ boards. It also identifies coincidence events based on the timestamp of the single events and transfers them to a PC through a 1-gigabit per second (Gbps) Ethernet.

Low voltages and a single high voltage for SiPM biasing are delivered to each sector using a digitally controlled power supply unit (iVS1, Artesyn Embedded Power) through a 20-m shielded power cable. The linear dropout (LDO) chips embedded in the front-end DAQ board subsequently regulate the low voltages for FPGAs. During the simultaneous PET/MRI studies, the power supply unit was located inside the MRI room [45] with a 20-m distance from the PET insert.

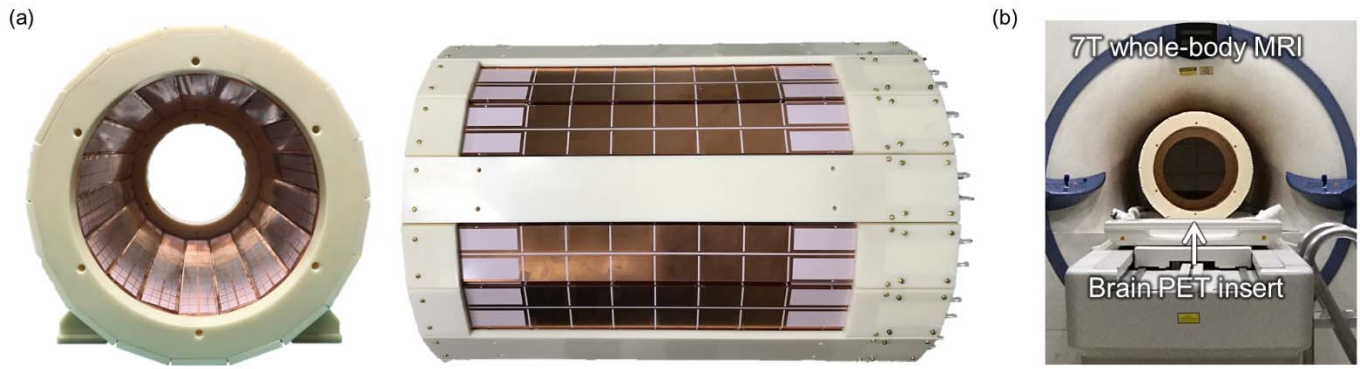


Fig. 1. Brain PET insert with MRI compatibility. (a) Prototype brain PET scanner. (b) PET scanner inserted within a 7T MRI scanner.

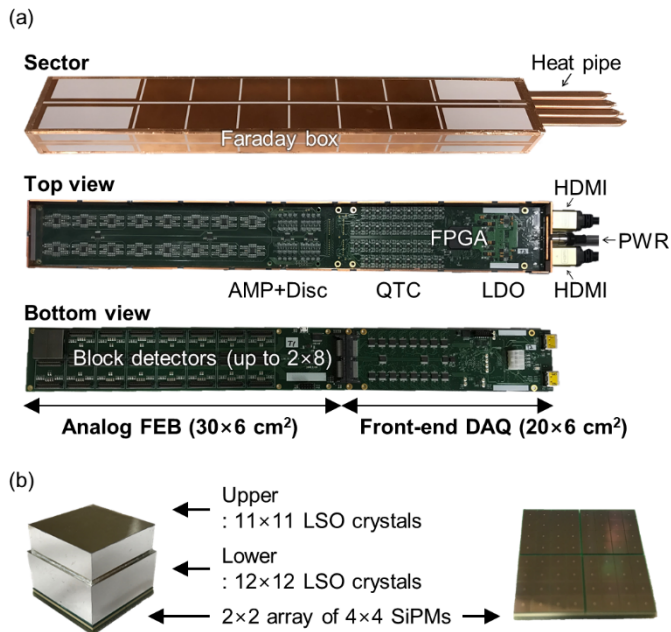


Fig. 2. Sector comprising block detectors, an analog front-end board (FEB), and a front-end data acquisition (DAQ) board. (a) Sector housed in a Faraday box. The FPGA digitizes the block detector signals and transfers digitized PET data to the back-end DAQ system through HDMI cables. All components of the sector are non-magnetic and linear drop-out (LDO) regulators are used for power distribution. (b) Block detector comprising two-layer crystal arrays and a 2×2 array of 4×4 SiPMs.

A liquid cooling system is used to regulate the temperature of the FPGA below 36°C . A chiller (Minichiller 600 OLE, Huber) supplies a coolant with a temperature of 15°C to aluminum heat sinks thermally coupled with four heat pipes. The heat pipes are thermally connected to the main active components in both analog FEBs and front-end DAQ boards (i.e. amplifiers, comparators, FPGA, etc.) via thermally conductive pads (PK605, LiPOLY).

A custom-made 8-channel transmit/receive (TX/RX) proton RF coil was utilized for the simultaneous PET/MRI study. The RF coil array is structured with a cylindrical acrylic former, featuring a diameter of 28.0 cm and a length of 19.0 cm. Each RF element features a rectangular structure of $150 \times 90 \text{ mm}^2$ using a flexible PCB, nonmagnetic capacitor (Dalicap), and

RG-316 nonmagnetic coaxial cable (Thermal Wire and Cables) (Fig. 4a). An 8-channel RF circuitry is equipped with preamplifiers and TX/RX switches and encapsulated in an acrylic box (Fig. 4b). The RF coil array was placed between the PET insert and a gradient coil of the 7T MRI scanner. The RF coil was tuned to the Larmor frequency of the 7T MRI system, corresponding to 297 MHz.

Table I summarizes the main characteristics of the developed brain PET/MRI system.

B. Block Detector

The high-resolution block detector comprises a two-layer stacked crystal array coupled with a SiPM array, as illustrated in Fig. 2(b). The upper layer is an 11×11 array of $2.09 \times 2.09 \times 8 \text{ mm}^3$ lutetium oxyorthosilicate (LSO) crystals (Sichuan Tianle Photonics), and the lower layer is a 12×12 array of $2.09 \times 2.09 \times 12 \text{ mm}^3$ LSO crystals. All crystal surfaces are mechanically polished, and enhanced specular reflector (ESR, 3M) films with a thickness of $65 \mu\text{m}$ are inserted between the LSO crystals for optical isolation. The crystal pitches for both the upper- and lower-layer crystals are 2.17 mm.

An optical grease (BC-630, Saint Gobain) is used to enhance the optical coupling between the crystal block and SiPM array. The PVC heat shrinkable wrap is used to fix the crystal array to the SiPM array. The SiPM array comprises a 2×2 array of 4×4 SiPMs (S13361-3050NE-04, Hamamatsu Photonics K.K (HPK)). The cross-sectional area of the block detector is $26.2 \times 26.2 \text{ mm}^2$. Further, the 64 SiPM anode signals are reduced into the four energy signals using a resistive charge division circuit [46], [47]. The common cathode signal is used as a timing signal. The temperature sensor is mounted at the center of the SiPM detector board.

C. Analog Front-End Board (FEB)

The analog FEB can mount a maximum of 2×8 block detectors to have an axial coverage of 22.4 cm. In this study, we mounted 2×6 block detectors in the PET scanner, which covers an axial length of 16.7 cm. The analog FEB has a dimension of $30 \times 6 \text{ cm}^2$ and consists of amplifiers (AMPs), voltage discriminators (Discs), and digital-to-analog

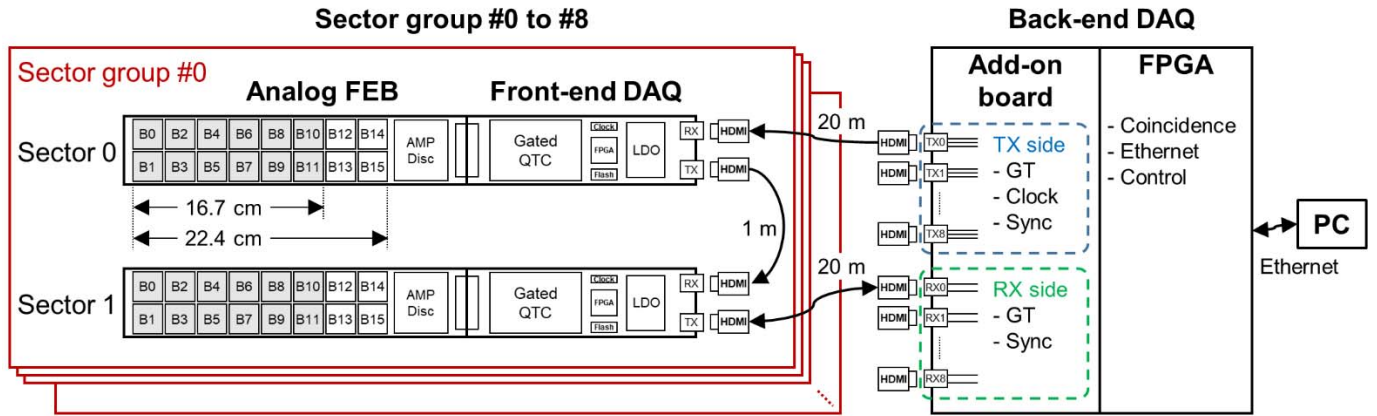


Fig. 3. Overview of the brain PET insert and the back-end DAQ system. The PET insert comprising nine sector groups, and each sector group consists of two sectors. Each sector can mount up to 2×8 block detectors with an axial length of 22.4 cm; however, only 2×6 block detectors (shaded in gray) with an axial length of 16.7 cm were implemented. Each sector group is connected with a back-end DAQ system using a pair of HDMI cables for PET data transfer and synchronization. The back-end DAQ system identifies and transfers coincidence events to a PC.

TABLE I

MAIN CHARACTERISTICS OF THE 7T BRAIN PET/MRI SYSTEM

Characteristics	Value
MRI Scanner	
Field strength	7 Tesla
Bore size	60 cm
Bed width	45.1 cm
RF coil	
Nucleus	^1H
Type	TX/RX coil
Number of channels	8
Diameter	28 cm
Length	19 cm
PET Scanner	
Inner Diameter	33.0 cm
Height	43.7 cm
Transverse FOV	25.6 cm
Axial FOV	16.7 cm
Number of sectors	18
Block detector	
Crystal material	LSO
Crystal dimension (upper layer)	$2.09 \times 2.09 \times 8 \text{ mm}^3$
Crystal dimension (lower layer)	$2.09 \times 2.09 \times 12 \text{ mm}^3$
Crystal array (upper layer)	11×11
Crystal array (lower layer)	12×12
SiPM active area/sensor pitch	$3 \times 3 \text{ mm}^2/3.2 \text{ mm}$
SiPM array per block detector	2×2 array of 4×4 SiPMs
Analog FEB	
Number of block detectors per sector	2×6 (transverse \times axial)
Energy signal multiplexing ratio	64:4
Timing signal multiplexing ratio	64:1
Front-end DAQ board	
Number of energy channels	64 (multiphase counters)
LSB of energy channels	625 ps
Number of timing channels	16 (TDCs)
LSB of timing channels	16 ps
Data rate of serial link	1.6 Gbps = 10 Mcps
Back-end DAQ system	
Number of gigabit transceivers	9 TX, 9 RX
Data rate of gigabit transceivers	1.6 Gbps = 10 Mcps
Data rate of Ethernet	1.0 Gbps

converters (DACs), as depicted in Figs. 2(a) and 3. The four energy signals from each block detector are amplified using a four-channel AMP (OPA4684, Texas Instruments). The

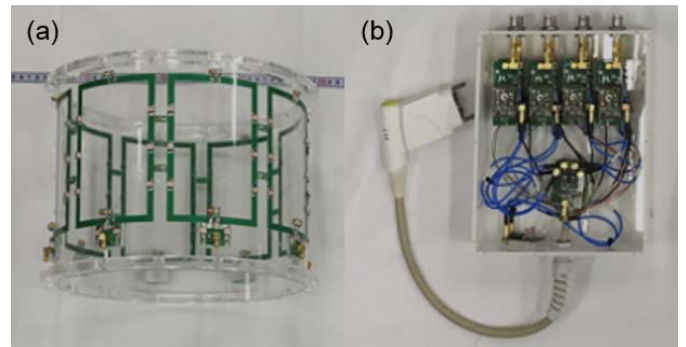


Fig. 4. RF coil for the developed brain PET/MRI system. (a) Custom-made 8-channel RF coil array. (b) 8-channel RF circuitry that includes preamplifiers, TX/RX switches, and phase shifter.

timing signal is amplified by a fast AMP (AD8000, Analog Devices) and then discriminated using a voltage comparator (ADCMP601, Analog Devices). The DAC (AD5629R, Analog Devices) is used to adjust the bias voltage of SiPMs and threshold voltage for the timing signals. A microcontroller unit (ATmega128A, Atmel) monitors the temperature of the detector board and controls the DAC to adjust the SiPM bias voltage to compensate the temperature-dependent gain variation of the SiPM [26]. The analog FEB is connected to the front-end DAQ board through 120-pin board-to-board connector pairs (QTH-060-01-F-D-RA, QSH-060-01-F-D-RA, Samtec).

D. Front-End Data Acquisition (DAQ) Board

The front-end DAQ board has a dimension of $20 \times 6 \text{ cm}^2$ and comprises a low-cost Artix-7 FPGA (XC7A100T-FG484, Xilinx), gated charge-to-time converter (QTC), power management integrated circuits (PMICs), clock distributors (CDCLVD1204, Texas Instruments), and other auxiliary discrete circuits, as depicted in Figs. 2(a) and 3. The PMIC comprises multiple LDOs (TPS7A85 and TPS7A88, Texas Instruments) and a sequencer (LM3880, Texas Instruments).

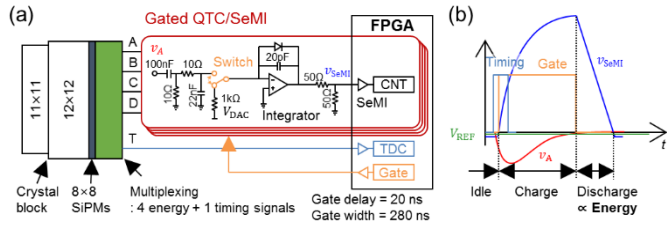


Fig. 5. Gated charge-to-time converter (QTC) combined with the single-ended memory interface (SeMI) input receiver of the FPGA. (a) Schematic. (b) Waveform.

The four gated QTCs consist of two dual-channel AMP (AD8066, Analog Devices), four Schottky diodes (1PS10SB82, Nexperia), a four-channel switch (ADG734, Analog Devices), and a DAC (AD5671R, Analog Devices). The time-to-digital converters (TDCs) and serial GTs are implemented within the FPGA.

The front-end FPGA DAQ board includes 64 energy and 16 timing channels and can digitize signals from up to 2×8 block detectors. The energy channel is a comparator-less gated QTC that combines a gated QTC with a SeMI input receiver (Fig. 5). The operating principle is almost identical to the comparator-less non-gated QTC [43] and a gate is added to improve the energy linearity despite the circuit complexity. The gated QTC generates the output pulse, whose pulse width at the discharge phase is proportional to the input charge. The attenuated dual-slope pulse is directly digitized by the FPGA using the SeMI input receiver and a multiphase counter (CNT) with a least significant bit (LSB) of 625 ps.

The timing channel is a tapped-delay-line TDC, comprising a 16-bit binary counter operating at 400 MHz and a 180-tap delay line with a bin-width tuning method [48], [49]. The LSB is of 16 ps. The even-numbered front-end DAQ board receives a common clock signal of 200 MHz from the back-end DAQ system through the 20-m HDMI cable (NEXT-2020UHD4K, EzNet). The odd-numbered front-end DAQ board receives the buffered clock signal from the even-numbered front-end DAQ board in the same sector group through a 1-m HDMI cable (NEXT-2001UHD4K, EzNet). The synchronization signal to simultaneously reset the TDCs of the 18 front-end DAQ boards is fed from the back-end DAQ system through the 20-m HDMI cables.

The processed single event data, including sector ID, block ID, four energy (A, B, C, and D), and one timing (T) information, is transferred to the back-end DAQ system. A serial GT with a data rate of 1.6 Gbps is used. Further, the 8b/10b encoding is used for DC balance and the data packet size is 128 bits and the maximum count rate for the GT is 10 Mcps.

E. Back-End DAQ System

The back-end DAQ system is developed by mounting an add-on board to a Virtex-6 evaluation kit (ML605, Xilinx), as illustrated in Fig. 6. The add-on board includes a 200-MHz clock oscillator (SIT9120, SiTime), a 2:16 clock distributor (CDCLVD1216, Texas Instruments), a 1:18 fanout buffer (8SLVS1118, IDT), and 18 HDMI connectors (nine TXs

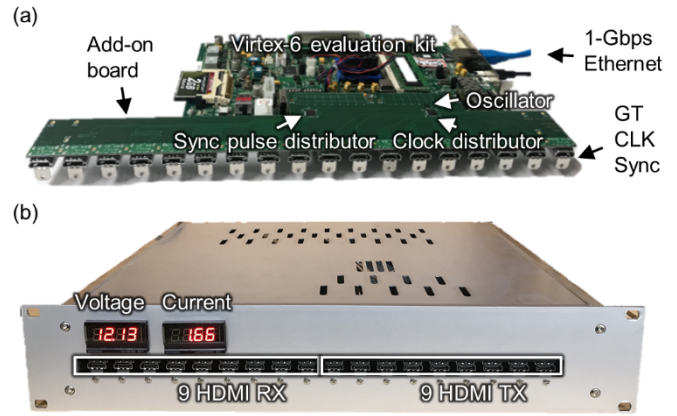


Fig. 6. Back-end FPGA DAQ system. (a) Virtex-6 evaluation kit connected with the add-on board to synchronize front-end DAQ boards and receive data. (b) Back-end FPGA DAQ system housed in a 19-inch 2U case.

and nine RXs). The 200-MHz clock signal generated by the clock oscillator is distributed to nine sector groups using the clock distributor through nine TXs. The synchronization pulse generated in the Virtex-6 FPGA is distributed to the 18 front-end FPGA DAQ systems using the fanout buffer through nine TXs and nine RXs.

The Virtex-6 evaluation kit includes nine GT TX and nine GT RX lanes and each of the TX and RX lanes is connected to the corresponding sector group. The back-end FPGA DAQ system receives unsorted PET data and identifies coincidence events based on the timestamps [50]. The coincidence events are transferred to the PC using the 1-Gbps Ethernet and the custom DAQ software was used to acquire PET data [26].

III. EXPERIMENTAL SETUP

A. Energy Linearity of the Front-End DAQ System

The linearity of the energy channel comprising the gated QTC and SeMI input receiver was evaluated by applying test pulses and varying the peak amplitude of exponential pulses. A digital detector emulator (DT5800D, CAEN) was used to generate the test pulses. The exponential pulses with a decay constant of 100 ns generated using the emulator were fed into the QTC while changing the peak amplitude from -0.4 to -3.2 V in steps of -0.4 V.

In this experiment, the feedback capacitor, DAQ output voltage, gate delay, integration width, and SeMI threshold voltage have the value of 100 pF, 0.5 V, 0 ns, 250 ns, and -40 mV, respectively.

A total of 50,000 events were collected for each measurement. The mean value and normalized full width at half maximum (FWHM) values were evaluated.

B. Timing Uncertainty of the DAQ System

The system-level timing uncertainty of the DAQ systems, including TDC, clock source, and clock distribution through the 20-m HDMI cables was evaluated. Digital pulses with fixed time differences ranging from 0 to 5.014 ns in steps of 501.4 ps were generated using the emulator and fed into the two TDC

channels in three different cases: 1) *reference*: single front-end DAQ board, 2) *intra-group*: two front-end DAQ boards in the same sector group, and 3) *inter-group*: two front-end DAQ boards in different sector groups.

For each measurement, 50,000 events were collected. The mean value and standard deviation (SD) values of the time difference were evaluated.

C. Performance Evaluation of the Block Detector

We obtained the flood map, energy resolution, and coincidence timing resolution (CTR) of the block detector using a coincidence measurement setup with a reference detector. We applied the baseline correction using the energy data obtained without source activity. We did not correct the SiPM saturation.

The reference detector was assembled with an R9800 PMT (HPK) coupled with a $4 \times 4 \times 10$ mm³ LYSO crystal [51]. A ²²Na point source was attached to the reference detector, and the distance between the block detector and the reference detector was 20 cm.

The crystal x , y positions and the energy E were calculated using pulse widths (PW) measured by four QTC channels, as described in the following equations:

$$x = \frac{-PW_A - PW_B + PW_C + PW_D}{E}, \quad (1)$$

$$y = \frac{+PW_A - PW_B - PW_C + PW_D}{E}, \quad (2)$$

$$E = PW_A + PW_B + PW_C + PW_D. \quad (3)$$

A total of 2,000,000 coincidence events were obtained and the photopeak events were used to evaluate the block detector performance. The flood map quality was assessed using the distance-to-width ratio (DWR) [43]. The energy resolution and CTR were evaluated after crystal identification.

D. Phantom Imaging Studies

We obtained several phantom images to demonstrate the imaging performance of the PET scanner. We used an in-house reconstruction software based on a line-of-response ordered subset expectation maximization (OSEM) [52] using a distance-driven projector [53]. The two-layer DOI information was compressed.

Direct normalization was performed using data from a ⁶⁸Ge cylindrical quality control (QC) phantom (EG-0318-2.5M, Eckert & Ziegler, Germany). Random correction was performed by subtracting delayed coincidence events from prompt coincidence events. Attenuation correction was performed using registered attenuation maps acquired from separate X-ray computed tomography (CT) scans.

We imaged a hot-rod phantom (ECT/DLX/MMP & ECT/HOT-MMP/I, Data Spectrum Corporation), a two-dimensional (2D) Hoffman brain phantom (BR/2D/P, Data Spectrum Corporation), and a three-dimensional (3D) Hoffman brain phantom (BR/3D/P, Data Spectrum Corporation). The hot-rod phantom has an inner diameter of 44 mm and a height of 34 mm. The six groups of hot rods have different diameters of 1.2, 1.6, 2.4, 3.2, 4.0, and

TABLE II
EXPERIMENTAL SETUPS AND RECONSTRUCTION
PARAMETERS FOR PHANTOM STUDIES

	Hot-rod phantom	2D brain phantom	3D brain phantom
Initial activity (mCi)	0.20	0.23	0.89
Scan time (h)	1	1	10
Total number of true coincidences	8.2 M	8.6 M	12.1 M
Iteration number	10	8	3
Number of subsets	18	18	18
Voxel size (mm ³)	0.54×0.54×5.45 (Axial Sum)	2.17×2.17×2.17 (Single Slice)	2.17×2.17×2.17 (Single Slice)
Gaussian post-filter kernel size (mm)	1.08	3.00	3.00

4.8 mm, respectively. The 2D Hoffman brain phantom has an inner diameter of approximately 20.0 cm. The 3D Hoffman brain phantom has an inner diameter of 20.8 cm and an axial length of 17.5 cm. All phantoms were filled with ¹⁸F-fluorodeoxyglucose (¹⁸F-FDG) solution. Table II summarizes the detailed scan and reconstruction parameters.

For the reconstructed hot-rod phantom image, we delineated one-dimensional (1D) profiles for the three smallest hot-rods (i.e. 1.2, 1.6, and 2.4 mm) and subsequently measured peak-to-valley ratios (PVRs) [43] to evaluate the image quality.

E. Performance Evaluation of the PET System

We evaluated the performance of the brain PET insert using both National Electrical Manufacturers Association (NEMA) NU 2-2018 (for clinical whole-body PET) and NU 4-2008 (for preclinical small-animal PET) standards because no NEMA standards dedicated for the brain PET scanner is currently available. The system performance was evaluated using an energy window of 350–650 keV and a fixed coincidence time-window of 4 ns, unless otherwise noted.

1) *Spatial Resolution*: The spatial resolution was measured based on the NEMA NU 4-2008 standard using a 0.25-mm diameter ²²Na point source embedded in a 1 cm³ acrylic cube (MMS-09-022, Eckert & Ziegler). The source was placed at the center of the transverse FOV and sequentially stepped in a radial direction up to 100 mm with a 5-mm interval. The measurement was performed at the axial center and repeated at the 1/4-axial-offset positions with no warm background. The acquired data were reconstructed using both a 2D filtered back-projection (FBP) and 3D OSEM (1 iteration and 18 subsets). A single-slice rebinning was applied before the 2D FBP reconstruction. The FWHM and the full width at tenth maximum (FWTM) values were evaluated.

2) *Sensitivity*: The sensitivity specified in the NEMA NU 4-2008 standard was measured using the same ²²Na point source utilized for the spatial resolution measurement. The source was placed at the center of the transverse FOV and axially stepped with a 2.17-mm interval to cover the entire axial FOV.

The sensitivity specified in the NEMA NU 2-2018 standard was also measured using an ^{18}F -FDG line source with five aluminum sleeves. The acquisition was repeated with the source axially shifted 0, 5, and 10 cm from the isocenter of the PET scanner. The sensitivity was then calculated by extrapolating the value for a hypothetical acquisition without aluminum sleeves after the decay correction. The background count rate was measured without the source and subtracted from each sensitivity measurement.

The sensitivity measurement was performed at three different energy windows of 250–750, 350–650, and 450–550 keV, respectively.

3) *Energy Resolution and CTR*: We preliminarily characterized the system-level energy resolution and CTR using a ^{22}Na point source located at the center FOV of the PET system.

F. Pilot Study of Simultaneous PET/MRI at 7 Tesla

As an initial step to demonstrate the feasibility of simultaneous PET/MRI, we acquired PET and MR data of a brain phantom filled with ^{18}F -FDG solution. The initial activity of ^{18}F -FDG was 1.33 mCi and the PET image was acquired at 1 hour after filling. For MR image acquisition, we applied a 3D gradient echo (GRE) pulse sequence with the following parameters: 8 ms echo time, 35 ms repetition time, 4 number of excitation, 30° flip angle, 130 Hz bandwidth per pixel, 3 mm slice thickness, $96 \times 96 \times 60$ matrix size. Total acquisition time of simultaneous PET/MRI was 13.5 min.

Also, a cylindrical phantom filled with corn oil was scanned with and without operating the PET system using the same GRE sequence inside the 7T MRI scanner. The MR images of the cylindrical phantom were then analyzed in terms of signal-to-noise ratio (SNR) and percent image uniformity (PIU) as described in the following equations:

$$\text{SNR} = 10 \cdot \log \left(0.655 \frac{\mu_s}{\sigma_n} \right) \text{ dB} \quad (4)$$

$$\text{PIU} = \left[1 - \frac{(S_{\max} - S_{\min})}{(S_{\max} + S_{\min})} \right] \times 100\% \quad (5)$$

In the equations, μ_s corresponds to the mean value of pixel intensity at a region-of-interest (ROI) drawn at the center of the phantom. σ_n corresponds to the standard deviation of pixel intensity measured within an ROI drawn at the background. S_{\max} and S_{\min} correspond to the maximum and minimum pixel intensity in the ROIs, respectively.

To further assess the effect of the MRI on PET, we compared PET count rates measured with and without applying the MRI pulse sequence (i.e. 3D GRE) used for simultaneous PET/MRI phantom imaging study. The PET count rate was measured with an ^{18}F point source (activity = 22.2 MBq) located at the center of FOV of the PET system.

IV. RESULTS

A. Energy Linearity of the Front-End DAQ System

The pulse width changed linearly with respect to the input peak amplitude as shown in Fig. 7(a). The R^2 value was 0.9999. The FWHM of the pulse width was less than 2% as shown in Fig. 7(b).

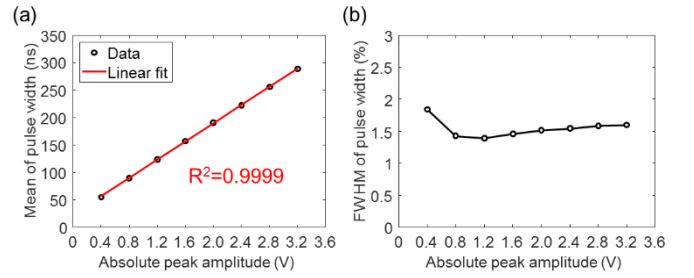


Fig. 7. Energy linearity test. (a) Mean value of the measured pulse width. (b) FWHM value of the measured pulse width.

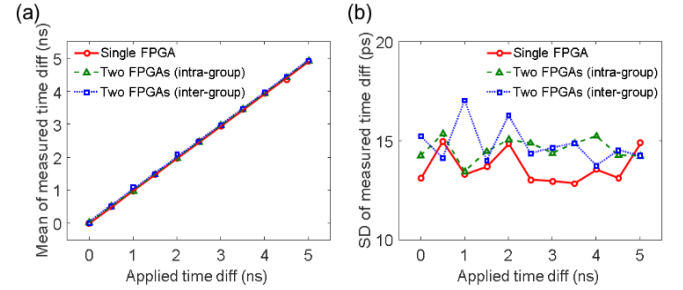


Fig. 8. Timing uncertainty measurement. (a) Mean value of the measured time difference. (b) Standard deviation value of the measured time difference.

B. Timing Uncertainty of the DAQ System

The mean values of the measured time differences were virtually identical to the applied time differences in all cases as shown in Fig. 8(a). The SD values of the measured time differences were less than 15.0, 15.4, and 17.0 ps in the *reference*, *intra-group*, and *inter-group* cases, respectively, as shown in Fig. 8(b).

C. Performance Evaluation of the Block Detector

All high-resolution crystals with two-layer DOI information were resolved in the flood map, as shown in Fig. 9(a). The DWR value between the upper- and lower-layer crystals was 3.2 ± 0.4 . The energy resolution values for the upper and lower layers were $9.2 \pm 0.7\%$ and $10.2 \pm 1.5\%$, respectively, as shown in Fig. 9(b). The CTR values were 492 ± 83 ps FWHM and 503 ± 96 ps FWHM, respectively, as shown in Fig. 9(c). As shown in Fig. 9(a), PET counts in the lower layer were fairly less than those in the upper layer, indicating that the length of crystals for each layer needs to be further optimized.

D. Phantom Imaging Studies

Fig. 10 shows the reconstructed image of the hot-rod phantom. The brain PET scanner could resolve the hot rod with a diameter of 1.6 mm in the reconstructed phantom image. The PVR values for the 1.2, 1.6, and 2.4-mm hot rods were 0.84, 1.38, and 3.11, respectively. Fig. 11(a) shows the reconstructed image of the 2D Hoffman brain phantom. The brain PET scanner could resolve the detailed brain structure. Fig. 11(b) shows the reconstructed image of the 3D Hoffman

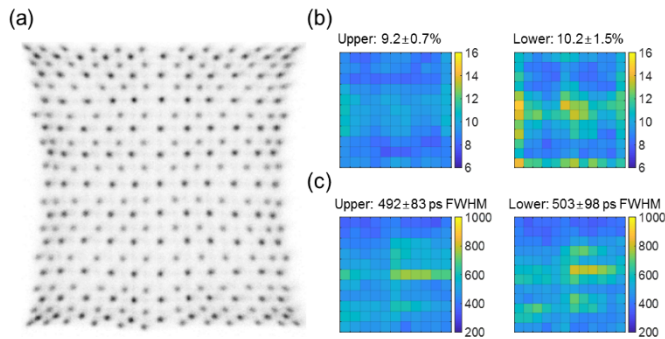


Fig. 9. Performance evaluation of the block detector. (a) Flood map. (b) Energy resolution. (c) CTR.

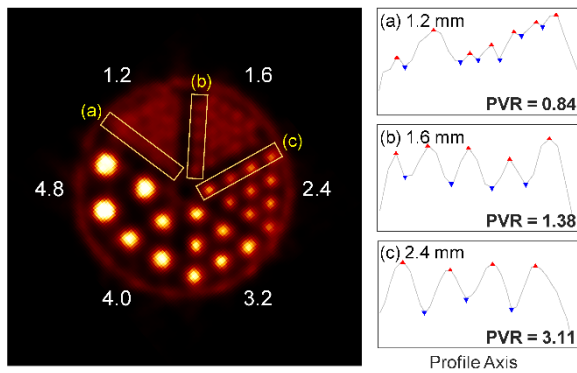


Fig. 10. Reconstructed hot-rod phantom image. The 1D profiles and PVR values are shown for three small hot rods with a diameter of (a) 1.2 mm, (b) 1.6 mm, and (c) 2.4 mm, respectively. The red and blue triangles represent peaks and valleys, respectively.

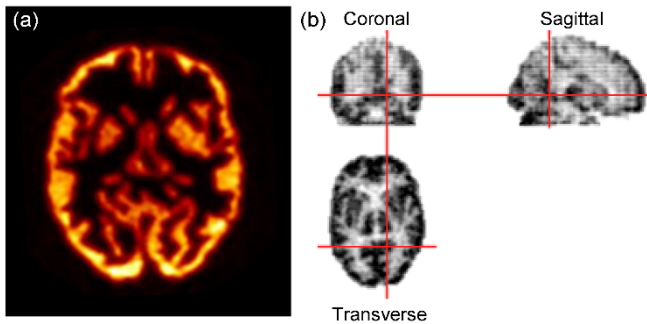


Fig. 11. Reconstructed phantom image of the (a) 2D Hoffman brain phantom and (b) 3D Hoffman brain phantom.

brain phantom. The brain PET scanner with an axial length of 16.7 cm was able to image the 3D brain phantom without bed movement.

E. Performance Evaluation of the PET System

1) *Spatial Resolution*: The spatial resolution measured at each source position is summarized in Tables III (2D FBP) and IV (3D OSEM). The radial/tangential/axial resolution at the center of the PET scanner was 2.53/2.51/2.28 mm FWHM (2D FBP) and 1.39/1.61/1.92 mm FWHM (3D OSEM).

2) *Sensitivity*: The axial sensitivity profiles at three different energy windows are illustrated in Fig. 12(a)-(c) (NEMA NU 2)

TABLE III
SPATIAL RESOLUTION AT AXIAL CENTER (2D FBP) SPATIAL RESOLUTION AT 1/4 AXIAL FOV FROM AXIAL CENTER (2D FBP)

Radial offset (mm)	Radial (R)		Tangential (T)		Axial (A)	
	FWHM (mm)	FWTM (mm)	FWHM (mm)	FWTM (mm)	FWHM (mm)	FWTM (mm)
0	2.53	4.44	2.51	5.59	2.28	5.21
5	3.32	6.58	2.92	7.80	2.47	5.83
10	2.53	4.44	3.09	7.62	2.41	5.38
15	2.56	4.59	2.94	6.43	2.59	5.66
25	2.55	4.53	3.48	7.05	3.10	6.33
50	2.83	5.66	3.18	7.03	5.16	8.61
75	3.16	8.41	3.58	8.31	7.58	11.18
100	3.36	10.12	4.15	9.64	9.21	13.24
120	4.58	19.14	4.67	9.87	9.95	14.42

Radial offset (mm)	Radial (R)		Tangential (T)		Axial (A)	
	FWHM (mm)	FWTM (mm)	FWHM (mm)	FWTM (mm)	FWHM (mm)	FWTM (mm)
0	2.74	4.73	2.50	5.35	2.34	5.28
5	3.10	5.44	2.99	7.51	2.46	5.68
10	2.53	4.39	3.19	7.25	2.47	5.31
15	2.55	4.57	2.88	6.35	2.62	5.45
25	2.65	4.74	3.52	6.93	2.98	5.78
50	2.81	6.16	3.26	7.08	4.05	7.10
75	3.14	8.18	3.62	8.41	5.18	10.15
100	3.40	9.51	4.22	9.61	6.26	12.50
120	4.23	11.51	4.58	10.08	7.03	14.63

TABLE IV
SPATIAL RESOLUTION AT 1/4 AXIAL FOV FROM AXIAL CENTER (2D FBP) SPATIAL RESOLUTION AT 1/4 AXIAL FOV FROM AXIAL CENTER (3D OSEM)

Radial offset (mm)	Radial (R)		Tangential (T)		Axial (A)	
	FWHM (mm)	FWTM (mm)	FWHM (mm)	FWTM (mm)	FWHM (mm)	FWTM (mm)
0	1.39	3.38	1.61	3.48	1.92	4.15
5	1.68	3.37	1.57	3.51	1.81	4.07
10	1.71	3.69	1.70	3.56	1.78	3.95
15	1.54	3.69	1.65	3.53	1.75	3.87
25	2.13	4.60	1.74	3.54	1.68	3.76
50	2.35	5.29	1.79	3.88	1.73	3.85
75	2.88	7.29	1.90	4.16	1.70	3.89
100	3.85	9.33	1.86	4.08	1.76	4.05
120	4.17	9.41	1.94	4.47	1.80	4.34

Radial offset (mm)	Radial (R)		Tangential (T)		Axial (A)	
	FWHM (mm)	FWTM (mm)	FWHM (mm)	FWTM (mm)	FWHM (mm)	FWTM (mm)
0	1.76	3.44	1.53	3.49	2.06	4.32
5	1.60	3.51	1.57	3.52	1.87	3.88
10	1.67	3.65	1.66	3.52	1.83	3.92
15	1.76	3.87	1.65	3.59	1.77	3.82
25	2.29	4.77	1.73	3.64	1.88	3.97
50	2.37	5.42	1.78	3.87	1.89	4.08
75	2.89	7.06	1.99	4.31	1.66	3.88
100	4.24	9.62	1.89	4.18	1.70	3.94
120	4.60	9.94	2.03	4.60	1.57	3.98

and (d) (NEMA NU 4). The NEMA NU 2 sensitivity measured at 0, 5, and 10 cm off-center was 38.2/41.0/44.7 kcps/MBq at the energy window of 250–750 keV, 18.9/20.6/23.7 kcps/MBq at the energy window of 350–650 keV, and 7.39/8.37/10.12 kcps/MBq at the energy window of 450–550 keV, respectively. The peak absolute sensitivity

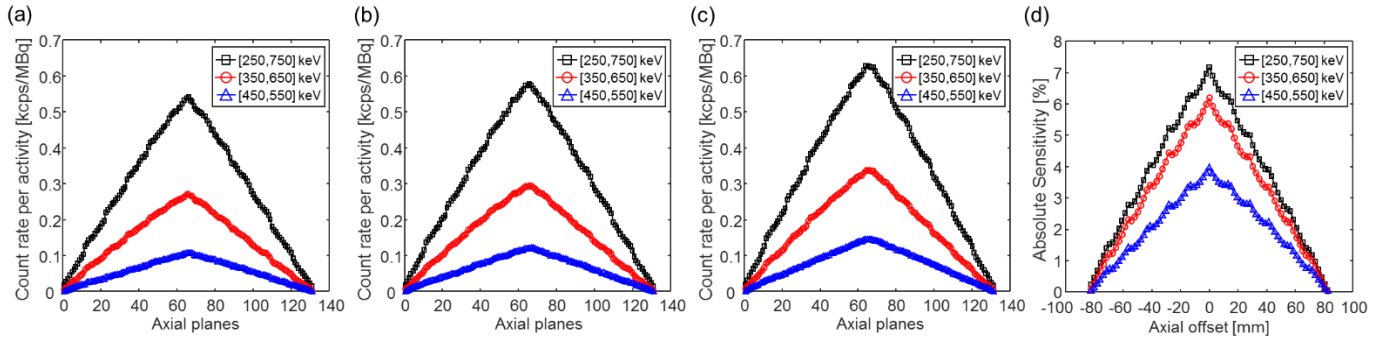


Fig. 12. NEMA NU 2 sensitivity measured at (a) 0, (b) 5, (c) 10 cm off-center, and (d) NEMA NU 4 sensitivity.

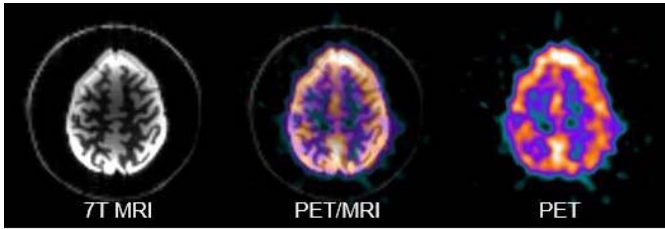


Fig. 13. Initial result of a simultaneous 7T PET/MRI using a Hoffman brain phantom.

measured at 250–750/350–650/450–550 keV was 7.17/6.19/3.96% according to the NEMA NU 4 standard.

3) *Energy Resolution and CTR*: The system-level energy resolution and CTR were $12.6 \pm 2.7\%$ and 1.21 ± 0.28 ns FWHM, respectively.

F. Pilot Study of Simultaneous PET/MRI at 7 Tesla

Fig. 13 shows our first simultaneous 7T PET/MRI result of the brain phantom. The initial results demonstrated a capability of simultaneous PET/MRI, showing that the ^{18}F -FDG distribution in the PET image well matches the brain structures visualized on the 7T MRI image. However, the PET image quality was not optimal. Unfortunately, we performed a system repair and replaced several block detectors between the simultaneous PET/MRI and normalization scans, causing the severe artifact in the PET image based on a 3D OSEM algorithm with normalization correction. Therefore, we applied a 2D FBP for PET image reconstruction without normalization.

In the 7T MRI image of the cylindrical phantom, no remarkable artifacts were observed during the PET operation, yielding the PIU value of 2.16% without the PET system and 2.87% with the PET system, respectively. However, the SNR of MR images in the uniform region decreased from 28.8 dB (without PET operation) to 15.8 dB (with PET operation). No remarkable PET count rate change was observed with and without applying the RF pulse sequence (Fig. 14).

V. DISCUSSION

In this study, we developed a brain PET insert using FPGA-only DAQ systems. The FPGA of the front-end DAQ board provided an all-in-one solution of signal digitization, high-speed data transmission, and slow control. The simplified DAQ

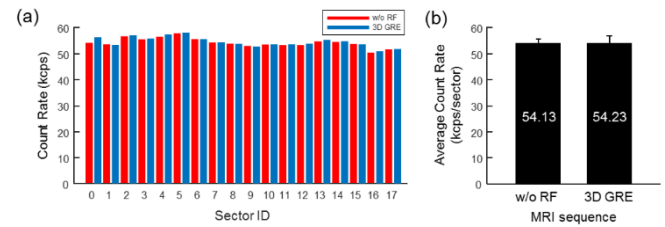


Fig. 14. PET count rate variation with and without applying MRI pulse sequence (a) Count rate variation for each sector. (b) Average count rate per sector.

electronics can be inserted in the Faraday box to digitize detector signals at their early stages and reduce the interconnection between the DAQ systems.

The energy channel was simplified by combining the gated QTC with the SeMI input receiver, as the FPGA replaced the gate generator and the voltage comparator that the gated QTC required. The input charge can be linearly measured using the energy channel, allowing for the crystal identification of high-resolution DOI-capable crystal arrays. Consequently, a spatial resolution of 2.5 mm was achieved at the center FOV and the hot rods with a diameter of 1.6 mm were resolved in the phantom study.

The timing channel was also simplified using the FPGA-TDC. The high-performance TDC with the LSB size of 16 ps and a low-jitter clock distribution system through 20-m HDMI cables enabled the system-level timing uncertainty of 17.0 ps.

Although the DAQ systems have a low timing uncertainty of 17.0 ps, the CTR value of approximately 500 ps FWHM was worse than that in our previous detector-level study [47], where we achieved the CTR values of 336 and 347 ps FWHM for upper- and lower-layer crystals, respectively. We consider that the narrow spacing between the fast timing signals due to the highly integrated circuit design of the current block detector degraded the timing resolution. Also, a light loss that occurred at a 0.2-mm gap between the 2×2 SiPM arrays may worsen the energy and timing resolutions of the PET detector, especially for the center crystals. We expect that the system-level timing performance can be further improved by individually optimizing several parameters (e.g. SiPM bias voltage and comparator threshold) per each sector along with the time-skew correction of the PET system.

TABLE V
SPATIAL RESOLUTION AT 1/4 AXIAL FOV FROM AXIAL CENTER (3D OSEM)

Brain PET Insert (Year)	Ring Diameter / Axial FOV (cm / cm)	Block Detector (Crystal, Photosensor)	Early Signal Digitization	Energy Window / Time Window (keV / ns)	Sensitivity (kcps/MBq)	Spatial Resolution (2D FBP)				MRI Field Strength
						@ (0, 0) mm		@ (100, 0) mm		
						R (mm)	T (mm)	R (mm)	T (mm)	
This work (2020)	33.0 / 16.7	Two-layer DOI (11×11+12×12) Upper crystal: 2.09×2.09×8 mm ³ Lower crystal: 2.09×2.09×12 mm ³ 8×8 SiPM arrays (HPK)	FPGA	350–650 / 4	18.9 (NU 2) 6.19% (NU 4)	2.53	2.51	3.36	4.15	7 Tesla
Siemens Brain PET (2012) [54]	32.0 / 19.1	No DOI (12×12) Crystal: 2.5×2.5×20 mm ³ 3×3 APD arrays (HPK)	-	420–600 / 12	7.2 (NU 2)	2.9*	1.8*	6.0	3.6	3 Tesla
Add-on PET (2017) [28]	24.8 / 12.0	Four-layer DOI (19×6×4) Crystal: 2.0×2.0×5.0 mm ³ 24×4 SiPM arrays (HPK)	-	-	-	2.3	-	3.5	-	3 Tesla
1st RF-penetrable PET (2018) [55]	32.0 / 28.0	No DOI, One-to-one coupling Crystal: 3.2×3.2×20 mm ³ 16×8 SiPM arrays (SensL)	-	410–610 / 10	-	-	-	-	-	3 Tesla
2nd RF-penetrable PET (2019) [33]	29.6 / -	No DOI, One-to-one coupling Crystal: 3.2×3.2×20 mm ³ 16×8 SiPM arrays (-)	PETA6-SE ASIC	-	-	-	-	-	-	3 Tesla
MINDView PET (2019) [3]	33.0 / 15.4	Monolithic (Four DOI bins) Crystal: 50×50×20 mm ³ 12×12 SiPM arrays (SensL)	-	350–650 / 5	7% (NU 4)	2.1*	1.5*	2.3	2.7	3 Tesla
TRIMAGE PET (2019) [32]	30.6 / 16.4	Two-layer DOI (7×7+8×8) Upper crystal: 3.3×3.3×8 mm ³ Lower crystal: 3.3×3.3×12 mm ³ 8×8 SiPM arrays (AdvanSiD)	TRIROC ASIC	350–650 / 3	-	-	-	-	-	1.5 Tesla

*Results obtained at position of (10, 0) mm

The combination of the FPGA and the HDMI cable allowed the reduction of the interconnection complexity. The analog signal was early digitized by the front-end DAQ board, and the digitized PET data were transferred to the back-end DAQ system through the serial GT and HDMI cable. The interconnection of the GT is also simple because each lane of the GT uses only a single pair of data lane. The receiver recovers the corresponding clock signal using the received data. The GT can be directly coupled with the copper media of the HDMI cable, which has five shielded twisted pairs. The common clock and synchronization signals were also distributed using the HDMI cable.

The combination of the FPGA-only DAQ system with the HDMI cable is also cost-effective. The costs of a front-end FPGA, a 1-m HDMI cable, and a 20-m HDMI cable were \$72, \$27, and \$3, respectively.

In the pilot simultaneous PET/MRI study, we observed a fairly significant drop in SNR of MR image (i.e. 28.8 dB to 15.8 dB) during PET operation. We consider that the loading effect of the PET insert may cause the degradation in the quality factor of RF coil. Also, incomplete RF shielding between PET and MRI may correspond to another reason for the SNR reduction. Therefore, an improved design of the RF coil and Faraday box is required to further reduce the loading effect and RF interference between PET and MRI. In this work, the simultaneous PET/MRI study was initially performed only using a 3D GRE sequence, which is the most commonly used for our 7T brain MRI studies, as it is faster and less sensitive to off-resonance than the spin echo imaging.

In the future investigation, we plan to conduct a more extensive testing of PET/MRI compatibility using various MRI pulse sequences with high duty cycles.

We evaluated the spatial resolution and sensitivity of the brain PET insert in accordance with the NEMA standards and compared its performance with those of other SiPM-based brain PET inserts developed for simultaneous PET/MRI. (Table V).

Nishikido *et al.* [28] developed an add-on PET that features four-layer DOI detectors mounted on the gaps between the RF coils. The four-layer DOI detector with four different reflector arrangements enabled them to achieve a good spatial resolution of less than 2.3 mm at the center FOV and less than 3.5 mm across the FOV. The add-on arrangement also reduces the PET ring diameter to improve the geometrical sensitivity by locating the RF coil between PET detectors. However, the sensitivity of the add-on PET was not reported.

Chang *et al.* [55] at Stanford University developed an RF-penetrable PET insert that allows the RF signal of the MRI body coil to penetrate the PET gantry. The PET insert uses an electro-optical coupling method and a battery power to separate the PET and MRI ground. A laser was used to convert the analog electrical signal to the analog optical signal. Energy resolution of 16.2% and CTR of 5.3 ns were achieved, but the spatial resolution and sensitivity were not evaluated. The second RF-penetrable PET insert is under development using the one-to-one coupling design and PETA6-SE ASIC to improve the timing resolution [33]. Although the PET scanner is not completely assembled, the detector-level study

showed good energy resolution and CTR of $13.66 \pm 0.08\%$ and 264.21 ± 4.82 ps FWHM, respectively.

Gonzalez *et al.* [3] developed a brain PET insert that can operate within a 3-Tesla MRI scanner, as a part of the MINDView project. The MINDView PET scanner was constructed using a monolithic crystal block with a virtual pixel size of 1.4 mm and a DOI bin size of 5 mm, thereby achieving a good spatial resolution of ~ 2 mm across the FOV. The MINDView brain PET scanner has a good sensitivity of $\sim 7\%$ (NEMA NU 4) owing to the use of monolithic crystals and a long axial coverage of 15.4 cm.

Belcari *et al.* [32] developed a brain PET scanner that can provide trimodal neurologic information of human brain along with MRI and electroencephalograms (EEGs), as a part of the TRIMAGE project. The block detector consisted of two-layer stacked crystals with a crystal pitch of 3.3 mm. The TRIROC ASIC was used to digitize PET signals at their early stages. The detector-level performance was reported with an energy resolution of 20–22% and CTR of 515 ps. The spatial resolution and sensitivity were not reported.

This work achieved spatial resolution and sensitivity comparable to those of state-of-the-art SiPM-based brain PET inserts with MRI compatibility. Although the detector board requires revision to improve the CRT, the brain PET scanner using high-resolution two-layer DOI-encoding crystals and FPGA-only signal digitization method showed a potential for simultaneous 7T brain PET/MRI with high sensitivity.

VI. CONCLUSION

In this study, we developed the 7T MRI-compatible brain PET insert based on the FPGA-only DAQ system and evaluated the PET performance in terms of spatial resolution and sensitivity using the NEMA NU 2 and NU 4 standards. We found that the simplified DAQ system was capable of digitizing all the SiPM signals from the brain PET scanner with an axial coverage of 16.7 cm. The interconnection using the HDMI cable provided a high-speed PET data transfer and low-jitter clock distribution. Moreover, the PET scanner equipped with high-resolution crystals achieved the spatial resolution of 2.5 mm FWHM (NEMA NU 4) at the center FOV and resolved hot rods with a diameter of 1.6 mm and the detailed structure of a 2D Hoffman brain phantom. The PET scanner with a 16.7-cm-long axial coverage achieved the peak sensitivity of 18.9 kcps/MBq (NEMA NU 2) and 6.19% (NEMA NU 4) and obtained the entire 3D Hoffman brain phantom without bed movement. Further studies will be conducted to improve the imaging performance of simultaneous 7T PET/MRI system, as well as TOF performance and MRI compatibility.

REFERENCES

- [1] C. Catana, "Development of dedicated brain PET imaging devices: Recent advances and future perspectives," *J. Nucl. Med.*, vol. 60, no. 8, pp. 1044–1052, Aug. 2019.
- [2] M. Watanabe *et al.*, "Performance evaluation of a high-resolution brain PET scanner using four-layer MPPC DOI detectors," *Phys. Med. Biol.*, vol. 62, no. 17, pp. 7148–7166, Aug. 2017.
- [3] A. J. Gonzalez *et al.*, "Initial results of the MINDView PET insert inside the 3T mMR," *IEEE Trans. Radiat. Plasma Med. Sci.*, vol. 3, no. 3, pp. 343–351, May 2019.
- [4] E. Berg *et al.*, "Development and evaluation of mini-EXPLORER: A long axial field-of-view PET scanner for nonhuman primate imaging," *J. Nucl. Med.*, vol. 59, no. 6, pp. 993–998, Jun. 2018.
- [5] S. R. Cherry, T. Jones, J. S. Karp, J. Qi, W. W. Moses, and R. D. Badawi, "Total-body PET: Maximizing sensitivity to create new opportunities for clinical research and patient care," *J. Nucl. Med.*, vol. 59, no. 1, pp. 3–12, Jan. 2018.
- [6] Y. Lv *et al.*, "Mini EXPLORER II: A prototype high-sensitivity PET/CT scanner for companion animal whole body and human brain scanning," *Phys. Med. Biol.*, vol. 64, no. 7, Mar. 2019, Art. no. 075004.
- [7] S. Surti, V. Viswanath, M. E. Daube-Witherspoon, M. Conti, M. E. Casey, and J. S. Karp, "Benefit of improved performance with state-of-the-art digital PET/CT for lesion detection in oncology," *J. Nucl. Med.*, vol. 61, no. 11, pp. 1684–1690, Nov. 2020.
- [8] C. S. Levin, S. H. Maramraju, M. M. Khalighi, T. W. Deller, G. Delso, and F. Jansen, "Design features and mutual compatibility studies of the time-of-flight PET capable GE SIGNA PET/MR system," *IEEE Trans. Med. Imag.*, vol. 35, no. 8, pp. 1907–1914, Aug. 2016.
- [9] J. van Sluis *et al.*, "Performance characteristics of the digital biograph vision PET/CT system," *J. Nucl. Med.*, vol. 60, no. 7, pp. 1031–1036, Jul. 2019.
- [10] J.-W. Son *et al.*, "Proof-of-concept prototype time-of-flight PET system based on high-quantum-efficiency multianode PMTs," *Med. Phys.*, vol. 44, no. 10, pp. 5314–5324, Oct. 2017.
- [11] W.-D. Heiss, "The potential of PET/MR for brain imaging," *Eur. J. Nucl. Med. Mol. Imag.*, vol. 36, no. S1, pp. 105–112, Mar. 2009.
- [12] S. Vandenberghe and P. K. Marsden, "PET-MRI: A review of challenges and solutions in the development of integrated multimodality imaging," *Phys. Med. Biol.*, vol. 60, no. 4, pp. R115–R154, Feb. 2015.
- [13] Y. Chen and H. An, "Attenuation correction of PET/MR imaging," *Magn. Reson. Imag. Clinics North Amer.*, vol. 25, no. 2, pp. 245–255, May 2017.
- [14] J. S. Lee, "A review of deep learning-based approaches for attenuation correction in positron emission tomography," *IEEE Trans. Radiat. Plasma Med. Sci.*, early access, Jul. 17, 2021, doi: 10.1109/TRPMS.2020.3009269.
- [15] Y. Shao *et al.*, "Simultaneous PET and MR imaging," *Phys. Med. Biol.*, vol. 42, no. 10, pp. 1965–1970, 1997.
- [16] S. Yamamoto *et al.*, "Simultaneous imaging using Si-PM-based PET and MRI for development of an integrated PET/MRI system," *Phys. Med. Biol.*, vol. 57, no. 2, pp. N1–N13, Jan. 2012.
- [17] M. S. Judenhofer *et al.*, "Simultaneous PET-MRI: A new approach for functional and morphological imaging," *Nature Med.*, vol. 14, no. 4, pp. 459–465, Apr. 2008.
- [18] C. Catana, Y. Wu, M. S. Judenhofer, J. Qi, B. J. Pichler, and S. R. Cherry, "Simultaneous acquisition of multislice PET and MR images: Initial results with a MR-compatible PET scanner," *J. Nucl. Med.*, vol. 47, no. 12, pp. 1968–1976, 2006.
- [19] S. J. Hong, H. G. Kang, G. B. Ko, I. C. Song, J.-T. Rhee, and J. S. Lee, "SiPM-PET with a short optical fiber bundle for simultaneous PET-MR imaging," *Phys. Med. Biol.*, vol. 57, no. 12, pp. 3869–3883, Jun. 2012.
- [20] S. J. Hong *et al.*, "An investigation into the use of geiger-mode solid-state photomultipliers for simultaneous PET and MRI acquisition," *IEEE Trans. Nucl. Sci.*, vol. 55, no. 3, pp. 882–888, Jun. 2008.
- [21] M. S. Judenhofer *et al.*, "PET/MR images acquired with a compact MR-compatible PET detector in a 7-T magnet," *Radiology*, vol. 244, no. 3, pp. 807–814, 2007.
- [22] B. Pichler *et al.*, "Performance test of a LSO-APD PET module in a 9.4 tesla magnet," in *Proc. IEEE Nucl. Sci. Symp. Conf. Rec.*, Nov. 1997, pp. 1237–1239.
- [23] H.-P.-W. Schlemmer *et al.*, "Simultaneous MR/PET imaging of the human brain: Feasibility study," *Radiology*, vol. 248, no. 3, pp. 1028–1035, Sep. 2008.
- [24] N. J. Shah, "Advances in hybrid MR-PET at 3T and 9.4T in humans," *Nucl. Instrum. Methods Phys. Res. A, Accel. Spectrom. Detect. Assoc. Equip.*, vol. 702, no. 21, pp. 16–21, 2013.
- [25] H. S. Yoon *et al.*, "Initial results of simultaneous PET/MRI experiments with an MRI-compatible silicon photomultiplier PET scanner," *J. Nucl. Med.*, vol. 53, no. 4, pp. 608–614, Apr. 2012.
- [26] G. B. Ko *et al.*, "Evaluation of a silicon photomultiplier PET insert for simultaneous PET and MR imaging," *Med. Phys.*, vol. 43, no. 1, pp. 72–83, Dec. 2015.

- [27] G. B. Ko *et al.*, "Simultaneous multiparametric PET/MRI with silicon photomultiplier PET and ultra-high-field MRI for small-animal imaging," *J. Nucl. Med.*, vol. 57, no. 8, pp. 1309–1315, Aug. 2016.
- [28] F. Nishikido *et al.*, "Development of a full-ring 'add-on PET' prototype: A head coil with DOI-PET detectors for integrated PET/MRI," *Nucl. Instrum. Methods Phys. Res. A, Accel. Spectrom. Detect. Assoc. Equip.*, vol. 863, no. 1, pp. 55–61, 2017.
- [29] N. Omidvari *et al.*, "PET performance evaluation of MADPET4: A small animal PET insert for a 7 t MRI scanner," *Phys. Med. Biol.*, vol. 62, no. 22, pp. 8671–8692, Nov. 2017.
- [30] M. Ahnen *et al.*, "Performance measurements of the SAFIR prototype detector with the STiC ASIC readout," *IEEE Trans. Radiat. Plasma Med. Sci.*, vol. 2, no. 3, pp. 250–258, May 2018.
- [31] P. Hallen *et al.*, "PET performance evaluation of the small-animal hyperion II d PET/MRI insert based on the NEMA NU-4 standard," *Biomed. Phys. Eng. Exp.*, vol. 4, no. 6, Oct. 2018, Art. no. 065027.
- [32] N. Belcari *et al.*, "Design and detector performance of the PET component of the TRIMAGE PET/MR/EEG scanner," *IEEE Trans. Radiat. Plasma Med. Sci.*, vol. 3, no. 3, pp. 292–301, May 2019.
- [33] Q. Dong *et al.*, "Characterization of TOF-PET detectors for a second generation radiofrequency-penetrable PET insert for simultaneous PET/MRI," in *Proc. IEEE Nucl. Sci. Symp. Med. Imag. Conf. (NSS/MIC)*, Oct. 2019, pp. 1–3.
- [34] F. Anghinolfi *et al.*, "NINO: An ultra-fast and low-power front-end amplifier/discriminator ASIC designed for the multigap resistive plate chamber," *Nucl. Instrum. Methods Phys. Res. A, Accel. Spectrom. Detect. Assoc. Equip.*, vol. 533, nos. 1–2, pp. 183–187, Nov. 2004.
- [35] A. D. Francesco *et al.*, "TOFPET2: A high-performance ASIC for time and amplitude measurements of SiPM signals in time-of-flight applications," *J. Instrum.*, vol. 11, no. 3, Mar. 2016, Art. no. C03042.
- [36] T. Harion *et al.*, "STiC—A mixed mode silicon photomultiplier readout ASIC for time-of-flight applications," *J. Instrum.*, vol. 9, no. 2, 2014, Art. no. C02003.
- [37] I. Sacco, P. Fischer, and M. Ritzert, "PETA4: A multi-channel TDC/ADC ASIC for SiPM readout," *J. Instrum.*, vol. 8, no. 12, Dec. 2013, Art. no. C12013.
- [38] J. Wu, Z. Shi, and I. Y. Wang, "Firmware-only implementation of time-to-digital converter (TDC) in field-programmable gate array (FPGA)," in *Proc. IEEE Nucl. Sci. Symp. Conf. Rec.*, Oct. 2003, pp. 177–181.
- [39] D. Xi, C.-M. Kao, W. Liu, C. Zeng, X. Liu, and Q. Xie, "FPGA-only MVT digitizer for TOF PET," *IEEE Trans. Nucl. Sci.*, vol. 60, no. 5, pp. 3253–3261, Oct. 2013.
- [40] M. Palka *et al.*, "Multichannel FPGA based MVT system for high precision time (20 ps RMS) and charge measurement," *J. Instrum.*, vol. 12, no. 8, Aug. 2017, Art. no. P08001.
- [41] Z. Zhao *et al.*, "An advanced 100-channel readout system for nuclear imaging," *IEEE Trans. Instrum. Meas.*, vol. 68, no. 9, pp. 3200–3210, Sep. 2019.
- [42] J. Y. Won and J. S. Lee, "Highly integrated FPGA-only signal digitization method using single-ended memory interface input receivers for time-of-flight PET detectors," *IEEE Trans. Biomed. Circuits Syst.*, vol. 12, no. 6, pp. 1401–1409, Dec. 2018.
- [43] J. Y. Won *et al.*, "Comparator-less PET data acquisition system using single-ended memory interface input receivers of FPGA," *Phys. Med. Biol.*, vol. 65, no. 15, Aug. 2020, Art. no. 155007.
- [44] B. J. Lee, R. D. Watkins, C.-M. Chang, and C. S. Levin, "Low eddy current RF shielding enclosure designs for 3T MR applications," *Magn. Reson. Med.*, vol. 79, no. 3, pp. 1745–1752, Mar. 2018.
- [45] Z.-H. Cho *et al.*, "A fusion PET–MRI system with a high-resolution research tomograph-PET and ultra-high field 7.0 T-MRI for the molecular-genetic imaging of the brain," *Proteomics*, vol. 8, no. 1, pp. 1302–1323, 2008.
- [46] S. Majewski, J. Proffitt, A. Stolin, and R. Raylman, "Development of a 'resistive' readout for SiPM arrays," in *Proc. IEEE Nucl. Sci. Symp. Conf. Rec.*, Oct. 2011, pp. 3939–3944.
- [47] H. Park and J. S. Lee, "Highly multiplexed SiPM signal readout for brain-dedicated TOF-DOI PET detectors," *Phys. Medica*, vol. 68, pp. 117–123, Dec. 2019.
- [48] J. Y. Won, S. I. Kwon, H. S. Yoon, G. B. Ko, J.-W. Son, and J. S. Lee, "Dual-phase tapped-delay-line time-to-digital converter with on-the-fly calibration implemented in 40 nm FPGA," *IEEE Trans. Biomed. Circuits Syst.*, vol. 10, no. 1, pp. 231–242, Feb. 2016.
- [49] J. Y. Won and J. S. Lee, "Time-to-digital converter using a tuned-delay line evaluated in 28-, 40-, and 45-nm FPGAs," *IEEE Trans. Instrum. Meas.*, vol. 65, no. 7, pp. 1678–1689, Jul. 2016.
- [50] J.-W. Son, J. Y. Won, and J. S. Lee, "Evaluation of a FPGA-based real-time coincidence system for high count rate PET scanners," in *Proc. IEEE Nucl. Sci. Symp. Med. Imag. Conf. (NSS/MIC)*, Oct. 2017, pp. 1–3.
- [51] M. Ito, J. P. Lee, and J. S. Lee, "Timing performance study of new fast PMTs with LYSO for time-of-flight PET," *IEEE Trans. Nucl. Sci.*, vol. 60, no. 1, pp. 30–37, Feb. 2013.
- [52] D. J. Kadmas, "LOR-OSEM: Statistical PET reconstruction from raw line-of-response histograms," *Phys. Med. Biol.*, vol. 49, no. 20, pp. 4731–4744, Oct. 2004.
- [53] B. D. Man and S. Basu, "Distance-driven projection and backprojection in three dimensions," *Phys. Med. Biol.*, vol. 49, no. 11, pp. 2463–2475, Jun. 2004.
- [54] A. Kolb *et al.*, "Technical performance evaluation of a human brain PET/MRI system," *Eur. Radiol.*, vol. 22, no. 8, pp. 1776–1788, Aug. 2012.
- [55] C.-M. Chang, B. J. Lee, A. M. Grant, A. N. Groll, and C. S. Levin, "Performance study of a radio-frequency field-penetrable PET insert for simultaneous PET/MRI," *IEEE Trans. Radiat. Plasma Med. Sci.*, vol. 2, no. 5, pp. 422–431, Sep. 2018.